Provided for non-commercial research and education use.
Not for reproduction, distribution or commercial use.

Volume 86, issues 2–3, March 2011
ISSN 0920-3796

ELSEVIER

Fusion Engineering and Design

An International Journal
for Fusion Energy and
Technology Devoted to Experiments, Analyses, Methods, and Designs

Principal Editor: Charles C. Baker
Editors: M.A. Abdou, P. Batistoni, O.G. Filatov, S. Konishi, G. Marbach,
W. Meier, A. Sagara; Emeritus Editors: R.W. Conn, C. Casini, G. Kulcinski,
P. Komarek, A. Miyahara, M. Ohta, K. Tomabechi

Research Articles

Non-axisymmetric magnetic field due to ferromagnetic inserts and helium cooled solid breeder test blanket modules in ITER, *D.K. Oh, H. Jhang, D.K. Lee, D.Y. Ku and S. Cho* 127
Feasibility study on cryogenic irradiation facility in JMTR, *Y. Inaba, K. Tsuchiya, T. Shikama, A. Nishimura and H. Kawamura* 134
Analysis of high β regimes for DEMO, *I.T. Chapman, R. Kemp and D.J. Ward* 141
New developments of the EAST data system, *L. Yang, L. Guiming, Z. Yingfei and L. Shi* 151
Boiling induced macroscopic erosion of plasma facing components in fusion devices, *Y. Shi, G. Miloshevsky and A. Hassanein* 155
Discrete magnetic probes measurement versus analytical method in determining plasma position in IR-T1 Tokamak, *A. Rahimi-Rad, M. Ghoranneviss and M. Emami* 163
Influence of multiple jet cooling on the heat transfer and thermal stresses in DEMO divertor cooling finger, *B. Končar, I. Simonovski and M. Draksler* 167
Conversion of plasma energy into electrical pulse by magnetic flux compression, *C.D. Sijoy and S. Chaturvedi* 174
Numerical simulation of MHD effects on convective heat transfer characteristics of flow of liquid metal in annular tube, *J.S. Rao and H. Sankar* 183
A study on influence of heat input variation on microstructure of reduced activation ferritic martensitic steel weld metal produced by GTAW process, *B. Arivazhagan, G. Srinivasan, S.K. Albert and A.K. Bhaduri* 192
Near-infrared detectors for ITER LIDAR Thomson scattering, *L. Giudicotti, R. Pasqualotto, A. Alfier, M.N.A. Beurskens, M. Kempenaars, J.C. Flanagan, M.J. Walsh and I. Balboa* 198
Assessment of tritium levels in rivers and precipitation in north-western Greece before the ITER operation, *K.C. Stamoulis, D. Karamanis and K.G. Ioannides* 206
Electromagnetic disruption analysis of 2.45 GHz LHW antenna in EAST under different plasma configurations, *J. Li and F. Liu* 214
Numerical assessment of functionally graded tungsten/steel joints for divertor applications, *T. Weber and J. Aktaa* 220
Fissile fuel breeding and minor actinide transmutation in the life engine, *S. Şahin, M.J. Khan and R. Ahmed* 227
Fabrication of multilayer graded density peeled-carbon-aerogel target, *Y. Zhong, B. Zhou, J. Gui, A. Du, Z. Zhang and J. Shen* 238
Design of neutral beam injection system for KSTAR tokamak, *D.H. Chang, S.R. In, K.W. Lee, J.T. Jin, D.S. Chang, S.H. Jeong, B.H. Oh, Y.S. Bae, Y.M. Park and H.L. Yang* 244

Errata

Erratum to "Thomson scattering upgrade on Tore Supra" [Fusion Eng. Des. 85 (2010) 335–339], *F. Leroux, L. Manenc and M. Moreau* 253
Erratum to "Thomson scattering upgrade on Tore Supra" [Fusion Eng. Des. 85 (2010) 335–339], *F. Leroux, L. Manenc and M. Moreau* 254

Available online at www.sciencedirect.com
ScienceDirect

This article appeared in a journal published by Elsevier. The attached copy is furnished to the author for internal non-commercial research and education use, including for instruction at the authors institution and sharing with colleagues.

Other uses, including reproduction and distribution, or selling or licensing copies, or posting to personal, institutional or third party websites are prohibited.

In most cases authors are permitted to post their version of the article (e.g. in Word or Tex form) to their personal website or institutional repository. Authors requiring further information regarding Elsevier's archiving and manuscript policies are encouraged to visit:

http://www.elsevier.com/copyright

Fusion Engineering and Design 86 (2011) 155–162

Contents lists available at ScienceDirect

Fusion Engineering and Design

journal homepage: www.elsevier.com/locate/fusengdes

Boiling induced macroscopic erosion of plasma facing components in fusion devices

Y. Shi*, G. Miloshevsky, A. Hassanein

School of Nuclear Engineering, Center for Materials under Extreme Environment, Purdue University, West Lafayette, IN 47907, USA

ARTICLE INFO

Article history:
Received 30 July 2010
Received in revised form 12 October 2010
Accepted 12 October 2010
Available online 8 December 2010

Keywords:
Plasma-facing component
Melt layer splashing
Boiling
Droplet
Macroscopic erosion
HEIGHTS

ABSTRACT

During plasma instabilities in tokamak devices, metallic plasma facing components (PFC) can undergo surface melting and vaporization. Macroscopic losses of melt layers developed during these instabilities are of a serious concern to the lifetime of PFC, the damage of nearby components, and potential core plasma contamination. Due to the presence of impurities and dissolved gas, boiling occurs in the superheated melt layer. The growing bubbles burst at the melt layer surface and induce the ejection of jet-droplets, therefore, contributing significantly to the erosion of PFC. In the present work, the boiling mechanism is investigated using a one-dimensional moving boundary model accounting for heating, melting, vaporization, and re-solidification. The collapse of a single bubble cavity and the jet formation, investigated numerically using computational fluid dynamics simulations, shows the amount of ejected jet-droplet is about ~1% of the initial bubble volume for liquid tungsten and aluminum. The intensity of boiling decreases with the pressure in the melt layer and increases with the incident heat flux. Simulations and experiments show similar results on the boiling characteristics of tungsten and aluminum. The simple and realistic model of the boiling induced erosion, presented here, allows better understanding of the mechanisms threatening the lifetime of the metallic PFC.

Published by Elsevier B.V.

1. Introduction

During normal and off-normal operations of current tokamak devices and future fusion reactors, the plasma facing components (PFC) are subjected to high-energy depositions (~10 to ~100 GW/m^2 during 0.1–1 ms) as a result of plasma instabilities such as disruptions, vertical displacement events, runaway electrons, and edge-localized modes (ELM) [1]. The thermal response of the metallic PFC includes melting and vaporization. Although the vapor-shielding phenomenon, i.e., accumulation of the material's own vapor cloud in front of the incoming plasma stream, considerably reduces the vaporized material losses from the surface [2], the continued plasma–target interaction can cause consequent damage to PFC due to macroscopic splashing of the developed melt layer, whose thickness is much larger than the net surface vaporization and can range from tens to hundreds of microns per one event of plasma instabilities [3]. An important mechanism inducing the erosion of the melt layer is attributed to the formation and bursting of bubbles during intense boiling near the surface region of the melt layer. This mechanism causes the continuous erosion of the molten PFC by the ejection of liquid droplets [4].

In order to simulate disruptions and ELMs with typical energy densities and pulse durations, which are not achievable in current tokamak devices, experiments using high power plasma accelerators are designed in laboratory facilities (e.g. VIKA, MK-200U, QSPA) in the frame of plasma–target interaction study [5,6]. Those experimental observations show the evidence of intense volumetric boiling in the re-solidified melt layer. Indeed, at VIKA facility [5], the surface of an aluminum target exposed to a plasma stream of 30 MJ/m^2 during 360 μs (square pulse) is covered by spherical dimples of 50–80 μm with a density of 1–2 mm^{-2} and droplets are observed in the peripheral regions of the heated target. A tungsten target also shows macroscopic erosion as well. However, presence of boiling is not specified. At TRINITI [6], aluminum and tungsten targets are exposed to multiple shots in the MK200-UG plasma gun with an energy density of 0.2–15 MJ/m^2 and a pulse-duration of 50 μs. For heat flux higher than 10 GW/m^2, the aluminum target shows bubble formation in a melt layer of 50–150 μm. At a maximum heat flux of 300–400 GW/m^2, cavities with typical diameters of 200–400 μm are observed. While no trace of boiling is present in the tungsten melt layer, 1–200 μm diameter droplets are seen in the erosion products. The experimental observations on tungsten demonstrated clearly that boiling is not the only melt layer erosion mechanism. Hydrodynamic instabilities could also contribute significantly to the splashing of the melt layer [4,7,8]. Therefore, efforts in the theoretical studies are crucial to the understanding of the bubble formation and bursting mechanisms and its quantitative contribution to the melt layer erosion.

---

* Corresponding author at: Potter Building, Purdue University, 400 Central Drive, West Lafayette, IN 47907-2063, USA. Tel.: +1 765 586 7245.
E-mail addresses: shi24@purdue.edu, yimeng.shi@mines.nancy-inpl.fr, mengmeng@gmail.com (Y. Shi).

0920-3796/$ – see front matter. Published by Elsevier B.V.
doi:10.1016/j.fusengdes.2010.10.002

The macroscopic erosion of the melt layer due to intense boiling is a complex phenomenon, which needs the integration of mechanisms governing both volumetric boiling in liquid metals and bursting of bubbles at a free surface. Little theoretical work was done to model this type of erosion in the frame of energetic heat deposition on metallic target. Boiling induced erosion of PFC was first implemented and modeled by Hassanein and coworkers [4] and integrated in the HEIGHTS simulation package as the module SPLASH [9]. The melt layer erosion was managed by the computation of an energy-based stationary splashing wave [4]. In reality, the droplet ejection due to bubble bursting at the free surface is a complex hydrodynamic problem, which has been extensively investigated for decades in the field of aerosol production in oceanographical studies [10]. The problem was also investigated numerically for the entrainment of radionuclide in accidental scenario in a nuclear reactor [11].

Two types of droplets are ejected during the free surface bubble bursting process: film-droplets due to the atomization of the thin liquid cap covering the bubble at the surface [12], and jet-droplets due to the disintegration of the liquid jet formed after the collapse of the remaining bubble cavity [13]. However, because film-droplets are relatively small (nano-scale) compared to jet-droplets (micro-scale) for water [13], the second mechanism is mostly investigated. The jet or jet-droplet formation was studied in other fields of application for similar mechanisms such as the Worthington jet induced by the impact of a falling drop on a free liquid surface [14] or the damage induced by the collapse of a cavitation bubble near a solid wall [15]. Thus, most results of jet-droplet formation are obtained for water. Liquid metals (e.g. tungsten or aluminum) are characterized by high surface tension and density (about one order of magnitude higher than the water properties), which are, according to parametric studies [16], the main properties controlling the jet-droplet formation. The same parametric studies provide more general results applicable to low viscosity materials. Meanwhile, those results mostly describe the early stage of the jet-droplet formation and cannot provide accurate information on the droplets from the disintegration of a fully developed jet.

In the present work, the macroscopic erosion of the melt layer due to intense boiling is investigated and modeled based on more detailed and realistic description of the physics driving both the formation of bubbles in the melt layer and the bursting mechanism leading to the ejection of jet-droplets. The model is based on the one-dimensional two-moving boundary model developed in [17–19], which describes the time-dependent thermal response of the metallic PFC exposed to intense heat deposition. The boiling induced erosion mechanism is modeled as the growth and bursting of successive bubble layers. The initiation and the velocity of bubble growth are computed dynamically. Computational fluid dynamics (CFD) simulations are performed to solve the two-phase flow problem of the jet-droplet formation in order to provide accurate information on the droplets. The amount of eroded material for a single bubble is generalized through the concept of “bubble layer” and integrated in the previously quoted moving-boundary model [17–19]. The simulation results using typical plasma characteristics from the laboratory experimental setup [5,6] are compared and discussed with the observations from the same experiments.

2. Physical model

2.1. Thermal response of PFC

Short duration and high heat flux plasma during disruptions and ELMs induce the heating, melting, and vaporization of the metallic PFC. These physical phenomena are described and modeled in detail using a one-dimensional two-moving boundary model [17,18]. Due to the vapor-shielding phenomenon, the incident heat flux is absorbed in the well-confined vapor layer on the target surface. Radiation transport simulation performed with HEIGHTS [20] shows that only 5–10% of the incident heat flux reaches the target surface when vapor shielding is effective.

2.2. Bubble growth dynamics

Boiling occurs due to heterogeneous nucleation. At first, the solid phase is filled with impurities, grain boundaries, radiation induced voids, thermal-stress induced cracks, etc., which play the role of heterogeneous nucleation sites for boiling. When the melt layer starts growing, vaporization and diffusion of dissolved second phase gas fill up the nucleation sites to form the initial micro-scale bubbles. Due to their relative small size, the trapped bubble is modeled as a sphere of radius R and its growth rate is assumed to have only a radial component dR/dt, which is a solution of the Rayleigh–Plesset equation with the inviscid fluid assumption [21]

$$R\frac{d^2R}{dt^2}+\frac{3}{2}\left(\frac{dR}{dt}\right)^2=\frac{1}{\rho_\mathrm{L}}\left[P_\mathrm{sat}(T)-\frac{2\sigma(T)}{R}-P_\mathrm{L}\right] \tag{1}$$

where ρ_L and P_L are respectively the density and the pressure of the melt layer. The vapor pressure inside the bubble at thermal equilibrium with the surrounding liquid, $P_\mathrm{sat}(T)$, is given by the Clausius–Clapeyron relation

$$P_\mathrm{sat}(T)=P_0\ \exp\left[\frac{L_\mathrm{v}}{\tilde{R}}\left(\frac{1}{T_\mathrm{b}}-\frac{1}{T}\right)\right] \tag{2}$$

where T_b is the boiling temperature (saturation temperature) at pressure P_0 equal to 1 atm, L_v is the latent heat of vaporization of the surrounding liquid and $\tilde{R}$ is the ideal gas constant. The temperature dependent surface tension, $\sigma(T)$ is defined as

$$\sigma(T)=\sigma(T_\mathrm{m})+\frac{d\sigma}{dT}(T_\mathrm{m}-T) \tag{3}$$

where T_m is the melting point of the PFC metal and $d\sigma/dT$ is a material dependent constant coefficient [22,23].

The spontaneous growth of the initial bubble is possible if the RHS of Eq. (1) is positive, i.e., the vapor pressure inside the bubble overcomes the surface tension and the surrounding liquid pressure

$$P_\mathrm{sat}(T)>\frac{2\sigma(T)}{R}+P_\mathrm{L} \tag{4}$$

The incident plasma stream compresses the melt layer during the heat deposition. Therefore, the pressure P_L within the melt layer is a parameter approximated to the values of the plasma pressure ranging from ~0.1 to ~10 atm [5] during the heat deposition. P_L drops to 0 when the heat deposition has ceased. Due to the relatively high surface tension of the liquid metal, the second term of the RHS of Eq. (1) plays an important role in the initiation of the bubble spontaneous growth. When $P_\mathrm{sat}(T)>P_\mathrm{L}$, the critical radius R_c is defined from Eq. (4) as

$$R_\mathrm{c}(T)=\frac{2\sigma(T)}{P_\mathrm{sat}(T)-P_\mathrm{L}} \tag{5}$$

Then, the spontaneous growth condition (Eq. (4)) of an initial bubble of radius R_0 is equivalent to $R_0>R_\mathrm{c}(T)$. The increase of the temperature induces the increase of the saturation pressure (Eq. (2)) and the decrease of the surface tension (Eq. (3)), and thus the decrease of the critical radius (Eq. (5)). Therefore, the spontaneous growth condition of Eq. (4) can only be achieved in the surface region of the melt layer where the temperature is the highest. The cooling effect at the bubble boundary due to vaporization is not significant as far as the bubble size is not large compared to the initial bubble size [24]. This condition is fulfilled due to the high surface tension of the liquid metal inducing a relatively high critical bubble radius. For example, if the excess of pressure $P_\mathrm{sat}(T)-P_\mathrm{L}$ has the typical value of ∼1 atm and the surface tension ∼1 N/m, then the critical radius is of the order of 20 μm. The simulation results presented later and the experimental observations [5,6] show a bursting bubble radius of ∼10 to ∼100 μm. In this case, the bubble growth is controlled by inertia and the growth rate is given by the Rayleigh solution [24]

$$\frac{dR}{dt} = \sqrt{\frac{2}{3\rho_L}\left[P_{sat}(T) - \frac{2\sigma(T)}{R} - P_L\right]} \qquad (6)$$

This solution can be derived from Eq. (1) by neglecting the first term of the LHS, which represents the growth acceleration. After the heat deposition has ceased, the vapor pressure only needs to overcome the surface tension to allow bubble growth. Because the initial bubble radius cannot be infinitely large, the fast decreasing temperature leads rapidly to $R_0 < R_c(T)$ and marks the end of boiling.

The effect of magnetic field on the bubble growth was not included in the present model. The analysis becomes more complicated due to the presence of an additional term in Eq. (1) reflecting the effect of the $J \times B$ force. Early theoretical analysis demonstrated that in the presence of magnetic field, the growing bubble deforms taking an elongated shape with its volume being less than that in the absence of magnetic field [25]. The rate of bubble growth may be also decreased [26].

2.3. Bubble layer and mass loss

In the current one-dimensional model, the growth of a single bubble is generalized to an entire bubble layer characterized by the same depth from the surface of the melt layer. The bubble density per unit area in this typical layer is estimated with the following energy balance

$$N = \frac{Q_{in} - Q_{out}}{Q_v + Q_\sigma - Q_P} \qquad (7)$$

where $Q_{in} - Q_{out}$ is the heat conducted through the bubble layer during the growth given by

$$Q_{in} - Q_{out} = \int_t \left[-k_L(T)\frac{\partial T_L}{\partial x}\bigg|_{in} + k_L(T)\frac{\partial T_L}{\partial x}\bigg|_{out}\right] dt \qquad (8)$$

where k_L is the temperature dependent thermal conductivity of the melt layer. The energy needed for the growth of a single bubble, $Q_v + Q_\sigma - Q_P$, is defined as

$$Q_v + Q_\sigma - Q_P = \int_t \left[4\pi R^2 \frac{dR}{dt}\rho_v L_v + 8\pi R\frac{dR}{dt}\sigma(T) - 4\pi R^2\frac{dR}{dt}(P_{sat}(T) - P_L)\right] dt \qquad (9)$$

where the terms are respectively the energy of vaporization, the surface energy, and the excess pressure energy. The vapor density ρ_v inside the bubble is given by the ideal gas law $\rho_v = P_{sat}(T)M/\tilde{R}T$ with M being the atomic weight. For simplification, the density of heterogeneous nucleation sites is assumed high enough not to affect the bubble density, which is only limited by the amount of available heat.

When the bubble boundary meets the surface of the melt layer, the bubble is assumed to burst and eject jet-droplets. Thus, the thickness of the eroded layer due to the bursting of one bubble layer is given by

$$\Delta X_{loss} = \frac{4}{3}\pi R^3 N \beta_R \qquad (10)$$

where the amount of eroded material for a single bubble is given as a fraction β_R of the bubble volume and it is determined in the jet-droplet formation studies by solving the two-phase flow equations using CFD simulations.

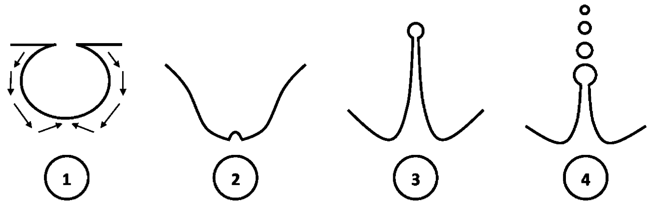

Fig. 1. Schematic representation of the jet-droplet formation mechanism.

The growth of a new bubble layer takes place immediately following the bursting of the previous one when the condition of Eq. (4) is fulfilled.

2.4. Bubble bursting and jet-droplet formation

When the boundary of the bubble meets the melt layer surface, the rupture of the film cap covering the bubble leaves a quasi-spherical cavity as represented in the step 1 of Fig. 1. Without considering any initial motion of the liquid, the surface tension tends to minimize the surface energy of the cavity, which is converted into the kinetic energy of the liquid confined in a boundary layer [13]. The convergence of the liquid in step 1 will induce the formation of a vortex ring at the base of the initial cavity and generate a high pressure gradient acting as the acceleration of the initial jet in step 2. In step 3, high inertia leads to a fully developed jet and eventually breaks into droplets in step 4 due to hydrodynamic instabilities.

The motion of the cavity is a free-surface two-phase flow problem and can be modeled by solving the mass and momentum conservation equations of the volume of fluid (VOF) model [27]. The energy equation is not considered here because the jet-droplet ejection mechanism is assumed isothermal in the current model. The liquid phase represents the liquid metal (melt layer). The gas phase can be either the vapor from the vaporization of the melt layer or the incident plasma heating the target. This choice does not affect the jet-droplet mechanism because the influencing factors are the properties of the liquid phase [16]. The volume fractions of the two phases satisfy $\alpha_L + \alpha_G = 1$. Far from the liquid–gas interface, the single-phase formulation is applied to each phase, i.e., in the liquid phase $\alpha_L = 1 + \varepsilon$ and in the gas phase $\alpha_G = 1 - \varepsilon$ with $\varepsilon \sim 10^{-8}$. The mass conservation equation is solved only for one phase (e.g. gas phase) in the form of a volume fraction equation

$$\frac{\partial \alpha_G}{\partial t} + \nabla\cdot(\alpha_G \vec{V}) = 0 \qquad (11)$$

where mass flux at the interface and other source terms are not considered because vaporization is assumed to have negligible impact on the jet formation mechanism. The volume fraction of the liquid phase is derived using $\alpha_L = 1 - \alpha_G$. The single velocity field $\vec{V}$ is obtained from one momentum conservation equation for the entire fluid domain

$$\rho\frac{\partial \vec{V}}{\partial t} + \nabla\cdot[\rho\vec{V}\vec{V} - \eta(\nabla\vec{V} + \nabla\vec{V}^T)] = -\nabla p + \vec{F}_\sigma \qquad (12)$$

where p is the single pressure field, ρ and η are the density and dynamic viscosity of the fluid domain. They are given as the volume-fraction-averaged values of the properties of each phase $(\rho, \eta) = \alpha_L(\rho, \eta)_L + \alpha_G(\rho, \eta)_G$. Using the continuum surface force (CSF) method [28], the effect of surface tension is modeled as a body force $\vec{F}_\sigma = \sigma\zeta\rho\vec{n}/[0.5(\rho_L + \rho_G)]$. The interfacial curvature is given by $\zeta = -\nabla\cdot(\vec{n}/|\vec{n}|)$ and the surface normal vector is defined as $\vec{n} = \nabla\alpha_G$. The constant value of the surface tension σ used in the CFD simulation is taken at the melting point of the metal $\sigma(T_m)$. The laminar flow assumption is justified by typical values of the Reynolds number lower than $\sim 10^3$. The incompressible fluid assumption is fully justified by a Mach number much lower than 0.3. The omission of the gravity term is justified by an Eötvös number of the order of 10^{-4}.

3. Numerical model

3.1. Integrated one-dimensional boiling model

The finite difference numerical scheme used to solve the time-dependent heat transfer and the two-moving boundary problems is described in detail in [19]. The one-dimensional grid has a resolution of 1 μm and the time-step is chosen small enough ∼1 ns to insure numerical stability.

If the condition of Eq. (4), evaluated at each time-step, is fulfilled, then the growth is initiated at a depth X_0 close to the melt layer surface where the temperature is the highest. The depth X_0 is chosen randomly between the melt layer surface X_{surface} and a maximum depth proportional to the melt layer thickness. Due to the thermal equilibrium assumption, the uniform temperature of the vapor inside the bubble is taken equal to the temperature of the melt layer at the depth X_0. The initial radius of the bubble is also chosen randomly within a range representing the size distribution of the heterogeneous nucleation sites. The growth rate of Eq. (6) is evaluated at each time-step and the bubble radius is computed using a forward scheme $R(t+\Delta t) = R(t) + \dot{R}(t+\Delta t)\Delta t$. If $R < R_c$, it is assumed the bubble layer will shrink and no bursting will occur. A new bubble layer is then created. Otherwise when $R \geq X_0 - X_{\text{surface}}$, the bursting condition is fulfilled. The bubble density given by Eq. (7) is computed as well as the thickness of the eroded material from Eq. (10). If the condition of Eq. (4) is still valid, a new bubble layer is created.

3.2. CFD simulation model

In order to determine β_R, the fraction of mass loss due to jet-droplet ejection per bubble, as well as parameters like the number of droplets, their size and their velocity, Eqs. (11) and (12) are solved using the VOF method. Since the fluid velocity field, computed from Eq. (12) with the pressure-based approach [29], does not satisfy Eq. (11), the pressure can be corrected using the Pressure-implicit with Splitting of Operators (PISO) method [30]. Both velocity and pressure are computed iteratively until the solution converges at the given time-step. The spatial discretization scheme used for the momentum equation is the third-order Monotone Upstream-centered Schemes for Conservation Laws (MUSCL) scheme [31], which improves spatial accuracy for all type of meshes by reducing the numerical diffusion. The pressure interpolation method to obtain face-centered values from the cell-centered values is the PREssure STaggering Option (PRESTO) [32]. The volume fraction equation (11) is discretized using the modified High Resolution Interface Capturing (HRIC) scheme [33], which is a stable and accurate numerical method for interface reconstruction. Finally, in order to insure numerical stability and optimize the computational cost, a variable time-advancing scheme is used based on a constant global courant number (chosen between 0.25 and 0.4). The computational software used in the present work is FLUENT, the commercial CFD simulation package.

A 2D axi-symmetric computational domain is generated using the grid generator GAMBIT. A user-defined function (UDF) is compiled in FLUENT to set up the initial phase separation. The initial geometry of the cavity is represented in Fig. 2, where the simulation domain is scaled for a bubble cavity of radius 100 μm. Due to the axis symmetry of the problem, the simulation domain is only half of the domain represented Fig. 2. In the direction of the axis of rotation, the computational domain is divided into 1200 uniform meshes (over 6 dimensionless unit length). In the radial direction, the domain is divided into 200 non-uniform meshes, whose sizes decreases when approaching the axis of rotation to insure square cells. The 240,000-cell grid is finer around the axis of rotation because higher values of the interfacial curvature is expected in this region due to the jet formation, which requires higher grid resolution. For example, if the grid is scaled for a cavity with 100-μm radius, the smallest cell size is 0.25 μm^2. A coarse grid with half of the number of divisions in each direction (i.e. 60,000 cells) is used only for the grid resolution convergence test.

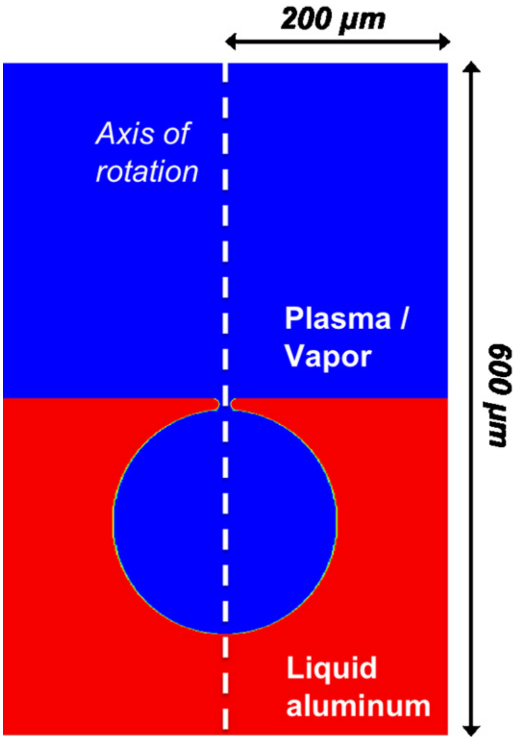

Fig. 2. Initial phase separation of the computational domain.

4. Results

4.1. Jet-droplet formation

The range of interest of the bubble radii is ∼10 to ∼100 μm according to experimental observations [5,6], which is consistent with the simulations results presented in Section 4.2. Therefore, the computational grid of the CFD simulation is scaled in this typical range. The simulations are performed with three fluids couples: air–water, plasma–tungsten and plasma–aluminum. Their properties are given in Table 1.

The convergence test is performed using a 100-μm air–water cavity with two grid-resolutions: 240,000 cells (fine grid) and 60,000 cells (coarse grid). The velocities of the ejected droplets are obtained for the two grid-resolutions and are plotted in Fig. 3. The probe located on the axis of rotation above the cavity measures the single velocity field of the entire fluid domain at this

Table 1
Fluid properties in CFD simulation.

Material	Air	Water	Plasma	Tungsten	Aluminum
ρ (kg/m^3)	1.2	998	$\sim 10^{-4}$	17,600	2375
η (kg/m s)	10^{-5}	10^{-3}	$\sim 10^{-5}$	0.007	0.0008
σ (N/m)		0.07		2.50	1.02

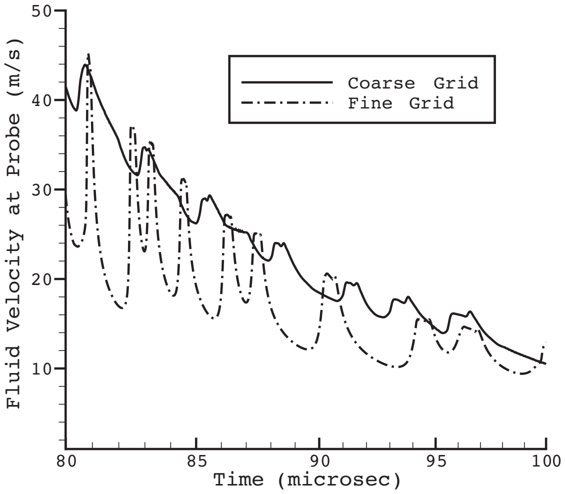

Fig. 3. Convergence test using the droplet velocity for 100-μm air–water cavity with two grid resolutions.

fixed point. On the higher resolution curve, each peak represents a droplet, which is not so obvious on the lower resolution curve. However, the droplet velocities on both curves match quite accurately. The simulation results in [16] reports a velocity of ~30 m/s for the first ejected droplet in the case of a 100-μm air–water cavity, which corresponds approximately to the velocity of the first droplet in Fig. 3. Furthermore, the number of droplets and their radii obtained with both grid-resolutions show good agreement. In the present work, only higher resolution (fine grid) results are reported.

Fig. 4 shows the jet-droplet ejection from the collapse of a 100-μm plasma–aluminum cavity. The deformation starts at the rim of the broken bubble, where the curvature is the highest (Fig. 4a). The deformation at the bottom of the cavity takes the typical cusp shape studied in [16], which is responsible for the trapping of the bubble at the cavity base (Fig. 4b). The trapped bubble follows the vertical motion of the same sinking vortex ring, which drives the formation of the jet. This typical motion is observed in the Indian ink experiment [13]. Because the acceleration is at maximum on the axis of rotation, the initial jet is relatively thin, which leads to a small droplet radius (Fig. 4c). The jet broadens with the radial diffusion of the velocity field leading to larger droplets (Fig. 4d).

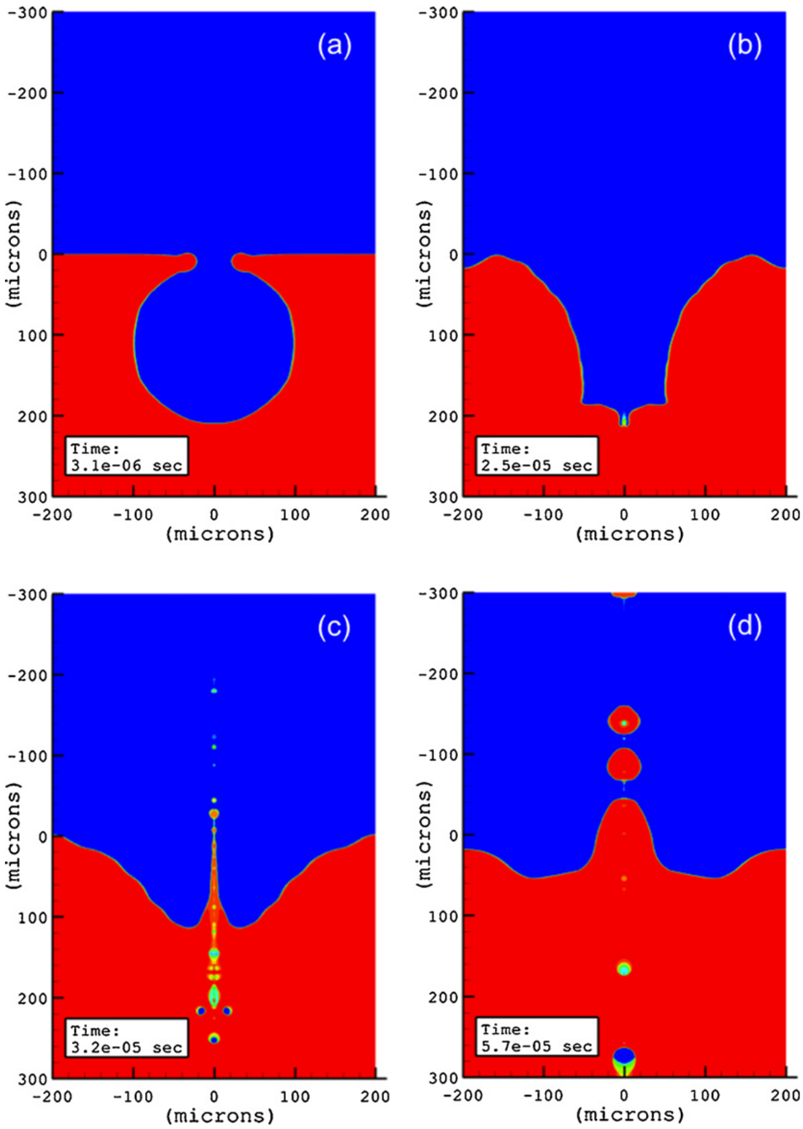

Fig. 4. Jet-droplet ejection from a 100-μm plasma–aluminum cavity: (a) rim deformation; (b) cusp formation at the cavity base; (c) jet initiation; and (d) fully developed jet and droplets ejection.

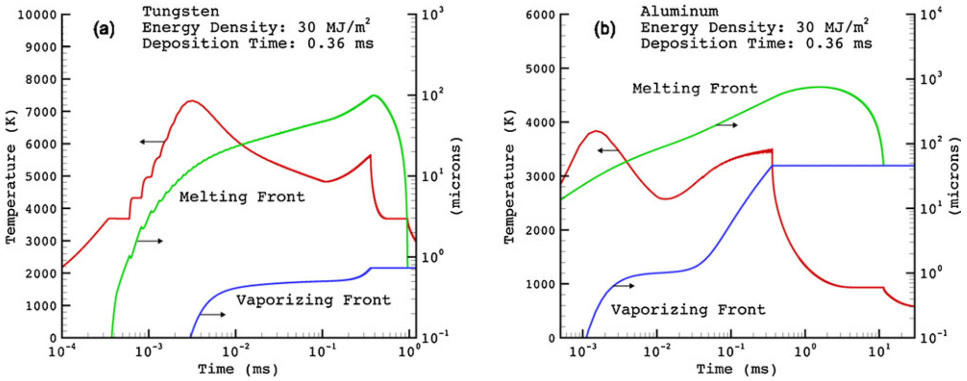

Fig. 5. Temperature profile, melting and vaporization fronts of (a) tungsten and (b) aluminum targets exposed to a surface heat density of 30 MJ/m^2 during 0.36 ms.

And the droplet production stops when the inertia of the jet is not high enough to overcome the surface tension effect.

The last statement is clearly observed in all the simulations performed on 50- and 100-μm cavities. The Weber number $We = \rho(R_\mathrm{d}V_\mathrm{d}^2)/\sigma$, where R_d and V_d are the radius and the velocity of the droplets (ρ and σ are defined in Eq. (12)), represents the competition between the inertia of the droplet and the surface tension effect on the formation of the droplet surface. The simulations show *We* decreases during the droplet production and the Weber number of the last droplet is right below 1.

The simulations of 50- and 100-μm cavities show the following results. For all materials, the number of ejected droplets per cavity is approximately 10. The range of the droplet radii for water is 2–10% of the initial bubble radius. This range for the two liquid metals is 2–20%. Then the total volume of ejected droplets per bubble is 0.3% of the initial bubble volume for water and 1% for the liquid metals. While the velocities of water droplet ranges from 1 to 30 m/s for the 100-μm bubble cavity, the liquid metal droplets can reach velocities up to 60 m/s (tungsten) and 90 m/s (aluminum). Reducing the bubble radius will increase the droplet velocities [16]. Using the velocities of the droplet, their radii and their number, it is possible to estimate the energy carried by the jet by summing the total surface energy and kinetic energy of the droplets. The results show that this energy is about 7% of the initial surface energy stored in the bubble cavity for water and 15% for the liquid metals, which is consistent with the 10–20% rule stated in [13]. Meanwhile for the 50-μm plasma–aluminum cavity, the results are slightly different. The number of ejected droplets, with radii ranging from 3 to 5 μm and velocities ranging from 20 to 65 m/s, is about 5, which yields an ejected volume of 0.3% of the bubble cavity volume and jet energy of 11% of the cavity surface energy. It is not clear why the ejected volume for the latter case is not of the order of 1%. This needs further investigation.

Since the width of the range of bubble radii is only one order of magnitude, it is fair to extrapolate the previous results to any bubble radius of this range. The fraction β_R of eroded volume per bubble given by Eq. (10) is equal to 0.01 for any bubble radius in both tungsten and aluminum. Due to the isothermal assumption stated in Section 2.4, the results presented in the current section apply to any range of heat flux and deposition time.

4.2. Bubble growth and mass loss

The parameters for plasma energy density and pulse duration used in the simulations are taken from typical experimental setups using VIKA (Efremov Institute) and MK200-UG (TRINITI) facilities. The long pulse quasi-stationary plasma gun at VIKA facility has an energy density up to 30 MJ/m^2 and pulse duration of 0.09–0.36 ms [5]. The MK200-UG plasma gun at TRINITI has an energy density up to 15 MJ/m^2 and pulse duration of 40–50 μs [6]. As in the experimental conditions, where the target are preheated, the initial temperature of the metal is set at 573 K.

The first series of results, obtained with the moving boundary thermal response model [17], uses plasma characteristics of VIKA experiments [5]. Fig. 5 shows the thermal response of tungsten (Fig. 5a) and aluminum (Fig. 5b) targets exposed to a 0.36-ms plasma pulse of 30 MJ/m^2. The melting front, i.e., the solid–melt front interface, the vaporizing front, i.e., the melt layer front surface, and as well as the surface temperature profile are plotted. For both metals, the surface temperature first increases rapidly due to the intense heat deposition. A melt layer starts to develop from the surface as soon as the surface temperature reaches the melting point. When the surface temperature of the melt layer continues to increase, intense vaporization is realized at the surface, which recedes as a vaporization front. The vapor builds up rapidly in front of the surface and induces a vapor-shielding mechanism that has the effect of reducing the incoming heat flux to 5% or 10% of its initial value according to detail modeling of HEIGHTS simulation package. In this simplified vapor shielding model, the aluminum vapor (low-Z material) is assumed to reduce the heat flux to 10%, whereas the tungsten vapor (high-Z material) will reduce the heat flux to 5%. When the decreasing heat flux reaches its constant value, the incoming radiation surface heat flux becomes higher than the heat lost through surface vaporization. Therefore the surface temperature is able to increase again. At 0.36 ms, the heat deposition ends and the heat losses through residual surface vaporization, radiation and conduction are responsible for the fast cooling of the melt surface. When the surface temperature is low enough, the surface vaporization becomes insignificant. However, the heat stored in the melt layer continues to be responsible for the growth of the melting front. Resolidification of the melt layer starts when the net heat flux through the melting front becomes negative. The surface temperature reaching the melting point implies the complete resolidification of the melt layer. Finally, the surface of resolidified target cools down through radiation and conduction. The plots show that melt layer is one to two orders of magnitude thicker than the vaporized layer. Aluminum is more volatile than tungsten with more than 40 μm is ablated by vaporization versus 1 μm of ablation for tungsten. Besides, the re-solidification time of the melt layer is much longer for aluminum, which means the aluminum melt layer has higher probability to be eroded by splashing mechanisms. Beryllium, which is a candidate PFC in future fusion devices, is expected to behave similar to aluminum targets in these experiments.

According to [5], the plasma stream pressure on the target varies from ~0.1 to 1 MPa. The parameter P_L (liquid pressure) is set at different values in the range 0.01–1 MPa to study its effect on boiling.

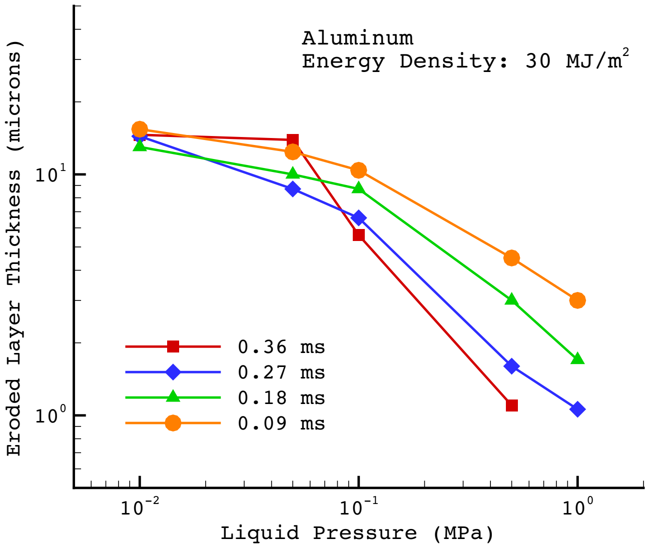

Fig. 6. Erosion of aluminum target due to boiling induced liquid splashing under a surface heat density of 30 MJ/m^2 for different deposition durations and different pressures applied to the liquid.

For different pulse durations at the same energy density (different heat fluxes), several characteristics numbers are computed: the total number of successive bubble layer bursts, the average number of bubble density (Eq. (7)), the average bubble radius, the average bubble growth rate and the thickness of ablated layer due to boiling induced droplet ejection. The thickness of ablation is plotted in Fig. 6. Increasing the heat flux from 80 GW/m^2 to 330 GW/m^2 tends to increase the average bubble density from ~50 mm^{-2} to ~800 mm^{-2}. For these specific ranges of heat flux and deposition time, the total number of successive bubble layer burst remains in the range of ~100–200. The growth rate increases with higher heat fluxes from 5 m/s to 15 m/s. Also, the increase of heat flux accelerates the advancement of the vaporizing front. Thus, the boundary of the growing bubble will meet the melt layer surface faster and burst with a smaller radius. Therefore, the average radius of the bursting bubble is decreased from ~30 μm to ~15 μm. The eroded amount of material is not affected by the variation of pulse duration (or heat flux) when the pressure applied to the melt layer is relatively low ~0.01 MPa because the increase in bubble density counteracts the decrease in bubble radius. When increasing the liquid pressure, there is a general decrease of the amount of eroded material because the vapor pressure inside the bubble needs to overcome a higher barrier to allow spontaneous growth. At 1 MPa and 0.36 ms, no boiling is observed. Besides, at higher liquid pressure, the increase of heat flux also increases the amount of eroded material because the effect of increasing bubble density prevails over the decrease of bubble radius. The range of bubble radii matches the experimental observations of 50–80 μm dimples [5].

For tungsten, using 0.01 MPa as liquid pressure, boiling occurs only for the lowest pulse duration 0.09 ms (highest heat flux) and the material loss is less than 1 μm. This is mainly because the vapor shielding effect is more effective for tungsten than for aluminum.

Using plasma characteristics of the MK200-UG plasma gun (0.2–15 MJ/m^2 with a duration of 50 μs), boiling does not occur in tungsten at the highest energy density, which is consistent with experimental observations [6]. In the case of aluminum at the highest energy density, the range of bubble radii is 5–100 μm, with an average bubble radius of 15 μm. Once again, the fast vaporization rate sets a limitation on the bubble radius. The maximum bubble radius is lower than the reported experimental values 200 μm [6]. Furthermore, the experimental observations provide a cut-off heat flux of 10 GW/m^2, above which significant boiling is observed in the aluminum melt layer. In the simulations using a negligible liquid pressure (0.01 MPa), the cut-off heat flux is about one order of magnitude higher.

5. Discussion

Some discrepancies exist and need further investigations. The relatively low values of material loss due to boiling (~1 to ~20 μm) first suggest that the jet-droplet ejection (~1% of the bubble volume) might not be the only droplet production mechanism during the bursting process. While the volume of film-droplets is negligible for small air–water cavity, the high surface tension of the liquid metal (>1 N/m) and the high growth rate of the bubble (5–15 m/s) could atomize the film cap before the thinning process takes place. A simple geometric estimation of the amount of liquid covering the upper half of the bubble provides a maximum volume of ~20% of the bubble volume, leading to considerable material loss.

Furthermore, boiling occurring after the heat deposition has ceased could explain the experimental observations of [34], where droplets were ejected during a relatively long period after the end of exposure to plasma. Due to the fast dropping vapor saturation pressure, this boiling period is relatively short. However, an additional pressure component in the bubble due to the presence of dissolved gas like hydrogen could extend the duration of this process. Besides, because intense vaporization has stopped, the growth of the bubble is not perturbed and could lead to larger bubble radius. The implementation of the additional partial pressure could also decrease the cut-off heat flux.

Finally, the bubble density computed using the energy balance could be overestimated. The 0.36-ms plasma pulse with an energy density of 30 MJ/m^2 induces a bubble density of 1–2 mm^{-2} in VIKA experiments, which is much lower than the computed value of ~50 mm^{-2}. However, it is worth noticing that the average bubble density of ~100 mm^{-2} computed using the energy balance for the typical average bubble radius of 10–50 μm corresponds to a target surface covered with a quasi-continuous bubble layer, which is observed in MK200-UG experiments. Meanwhile, the maximum bubble density of ~1200 mm^{-2} for the smallest bubbles is not observed. This could be due to the limitation of the nucleation site density in the real material.

6. Conclusion

The boiling induced macroscopic erosion mechanism of the metallic PFC during intense heat deposition was modeled in the present work. The boiling mechanism is integrated in a two-moving boundary code modeling the thermal response of the PFC including heating, melting, vaporization, and re-solidification phenomena. For the first time, the physics of the jet-droplet formation is investigated in the frame of bubble bursting at the free surface of a liquid metal. Using CFD simulations, detailed information is provided on the droplet characteristics (number, size, velocity). These results quantify accurately and realistically the amount of jet-droplet ejection from a single bubble with a given radius. Then this quantity, generalized and coupled to the model of successive growth and burst of bubble layers, provides the one-dimensional macroscopic erosion of the melt layer due to intense boiling.

Overall good agreement is found between the simulation results and the experimental observations of boiling in the PFC melt layer. In aluminum, boiling is more intense with increasing heat flux. Higher pressure in the melt layer reduces or suppresses the erosion due to boiling. The average bubble radius varies from 5 to 100 μm. The bubble density ranges from ~10 to ~1000 mm^{-2}. The discrepancies with experimental data suggest several investigations: the atomization mechanism of the liquid cap covering the bubble, the contribution of partial pressure of dissolved gas and the limitation of heterogeneous nucleation sites. Beryllium, which is a candidate PFC in future fusion devices, is expected to behave similar to aluminum. The presence of magnetic fields may affect the bubble growth mechanism and should be included as an additional term in Eq. (1).

The numerical and experimental observation of tungsten not affected by boiling except at very high heat flux (~300 GW/m^2) suggests that other mechanisms of melt layer splashing, such as hydrodynamic instabilities, will dominate and greatly contribute to the macroscopic erosion of PFC.

Acknowledgements

This work is supported by the U.S. Department of Energy, Office of Fusion Energy Sciences. TeraGrid computational resources provided by the NCSA under Grant TG-PHY090096. The authors acknowledge the NCSA for providing FLUENT software.

References

[1] G. Federici, Plasma wall interactions in ITER, Phys. Scr. T124 (2006) 1–8.
[2] A. Hassanein, Disruption damage to plasma-facing components from various plasma instabilities, Fusion Technol. 30 (1996) 713–719.
[3] A. Hassanein, V. Belan, et al., Modeling and simulation of melt-layer erosion during a plasma disruption, J. Nucl. Mater. 241–243 (1997) 288–293.
[4] A. Hassanein, A. Konkashbaev, I. Konkashbaev, Erosion of melt layers developed during a plasma disruption, Fusion Technol. 1 (1994) 223–226.
[5] V.N. Litunovsky, Study of material response on simulated ITER disruptive plasma heat load with variable duration, in: Proceedings of the 16th Symposium on Fusion Engineering, 1995, pp. 435–438.
[6] N.I. Arkhipov, et al., Material erosion and erosion products in disruption simulation experiments at the MK-200 UG facility, Fusion Eng. Des. 49–50 (2000) 151–156.
[7] G. Miloshevsky, A. Hassanein, Modeling of Kelvin-Helmholtz instability and splashing of melt layers from plasma facing components in tokamaks under plasma impact, Nucl. Fusion 50 (2010) 115005, doi:10.1088/0029-5515/50/11/115005.
[8] B. Bazylev, G. Janeschitz, I. Landman, et al., ITER transient consequences for material damage: modelling versus experiments, Phys. Scr. T128 (2007) 229.
[9] A. Hassanein, et al., Modeling and simulation of melt-layer erosion during a plasma disruption, J. Nucl. Mater. 241–243 (1997) 288–293.
[10] N. Reinke, Aerosol generation by bubble collapse at ocean surfaces, Water, Air, Soil Pollut.: Focus 1 (2001) 333–340.
[11] M.K. Koch, Radionuclide re-entrainment at bubbling water pool surfaces, J. Aerosol Sci. 31 (2000) 1015–1028.
[12] Y. Toba, Drop production by bursting of air bubbles on the sea surface (II) theoretical study on the shape of floating bubbles, J. Oceanogr. Soc. Jpn. 15–3 (1959) 121–130.
[13] F. MacIntyre, Bubbles: a boundary-layer microtome for micron-thick samples of a liquid surface, J. Phys. Chem. 72 (1968) 589–592.
[14] A.M. Worthington, On impact with a liquid surface, Proc. R. Soc. Lond. 34 (1883) 217–230.
[15] M.S. Plesset, R.B. Chapman, Collapse of an initially spherical vapor cavity in the neighborhood of a solid boundary, J. Fluid Mech. 47 (1971) 283–290.
[16] L. Duchemin, et al., Jet formation in bubbles bursting at a free surface, Phys. Fluids 14–9 (2002) 3000–3008.
[17] A.M. Hassanein, G.L. Kulcinski, Surface melting and evaporation during disruptions in magnetic fusion reactors, Nucl. Eng. Des. Fusion 1 (1984) 307–324.
[18] A.M. Hassanein, Response of Materials to Severe Heat Fluxes During Operation in Fusion Reactors, ASME, 1988, 88-WA/NE-2.
[19] A. Hassanein, On the numerical solution with applications to two moving boundary heat conduction problems, in: Proceedings of the ASME/JSME Thermal Engineering Joint Conference I0309A, 1991, pp. 245–252.
[20] A. Hassanein, et al., Materials effects and design implications of disruptions and off-normal events in ITER, Fusion Eng. Des. 39–40 (1998) 201–210.
[21] M.S. Plesset, S.A. Zwick, The growth of vapor bubbles in superheated liquids, J. Appl. Phys. 25–4 (1954) 493–500.
[22] Kh.Kh. Kalazhokov, Surface tension of pure aluminum melt, Tech. Phys. 48 (2003) 272–273.
[23] P.F. Paradis, T. Ishikawa, Thermophysical properties of molten tungsten measured with an electrostatic levitator, Heat Transfer – Asian Res. 35 (2006) 152–164.
[24] E. Sher, Flash-boiling atomization, Prog. Energy Combust. Sci. 34 (2008) 417–439.
[25] C.P.C. Wong, G.C. Vliet, P.S. Schmidt, Magnetic field effects on bubble growth in boiling liquid metals, J. Heat Transfer 100 (1978) 466–472.
[26] P. Lykoudis, Bubble growth in the presence of a magnetic field, Int. J. Heat Mass Transfer 19 (1976) 1357–1362.
[27] C.W. Hirt, Volume of fluid (VOF) method for the dynamics of free boundaries, J. Comput. Phys. 39 (1981) 201–225.
[28] J.U. Brackbill, D.B. Kothe, C. Zemach, A continuum method for modeling surface tension, J. Comput. Phys. 100 (1992) 335–354.
[29] A.J. Chorin, Numerical solution of Navier–Stokes equations, Math. Comput. 22 (1968) 745–762.
[30] R.I. Issa, Solution of implicitly discretized fluid flow equations by operator splitting, J. Comput. Phys. 62 (1986) 40–65.
[31] B. Van Leer, Towards the ultimate conservative difference scheme. V. A second-order sequel to Godunov's method, J. Comput. Phys. 32 (1979) 101–136.
[32] S.V. Patankar, Numercial Heat Transfer and Fluid Flow, Hemisphere, Washington, DC, 1980.
[33] S. Muzaferija, et al., A two-fluid Navier–Stokes solver to simulate water entry, in: Proceedings of the 22nd Symposium on Naval Hydrodynamics, Washington, DC, 1998, pp. 638–651.
[34] B. Bazylev, G. Janeschitz, Experimental and theoretical investigation of droplet emission from tungsten melt layer, Fusion Eng. Des. 84 (2009) 441–445.